THE UNIVERSITY OF RHODE ISLAND

University of Rhode Island
DigitalCommons@URI

Chemistry Faculty Publications

Chemistry

2004

Phase Changes in Selected Lennard-Jones $X_{13-n}Y_n$ Clusters

Dubravko Sabo

Cristian Predescu

See next page for additional authors

Follow this and additional works at: https://digitalcommons.uri.edu/chm_facpubs

Terms of Use
All rights reserved under copyright.

Citation/Publisher Attribution

Sabo, D., Predescu, C., Doll, J. D., & Freeman, D. L. (2004). Phase Changes in Selected Lennard-Jones $X_{13-n}Y_n$ Clusters. *Journal of Chemical Physics, 121*(2), 856-867. doi: 10.1063/1.1759625
Available at: http://dx.doi.org/10.1063/1.1759625

This Article is brought to you for free and open access by the Chemistry at DigitalCommons@URI. It has been accepted for inclusion in Chemistry Faculty Publications by an authorized administrator of DigitalCommons@URI. For more information, please contact digitalcommons@etal.uri.edu.

Authors
Dubravko Sabo, Cristian Predescu, J. D. Doll, and David L. Freeman

This article is available at DigitalCommons@URI: https://digitalcommons.uri.edu/chm_facpubs/12

HTML ABSTRACT + LINKS

JOURNAL OF CHEMICAL PHYSICS VOLUME 121, NUMBER 2 8 JULY 2004

Phase changes in selected Lennard-Jones $X_{13-n}Y_n$ clusters

Dubravko Sabo,[a] Cristian Predescu,[b] and J. D. Doll
Department of Chemistry, Brown University, Providence, Rhode Island 02912

David L. Freeman
Department of Chemistry, University of Rhode Island, Kingston, Rhode Island 02881

(Received 22 March 2004; accepted 19 April 2004)

Detailed studies of the thermodynamic properties of selected binary Lennard-Jones clusters of the type $X_{13-n}Y_n$ (where $n=1$, 2, 3) are presented. The total energy, heat capacity, and first derivative of the heat capacity as a function of temperature are calculated by using the classical and path integral Monte Carlo methods combined with the parallel tempering technique. A modification in the phase change phenomena from the presence of impurity atoms and quantum effects is investigated. © *2004 American Institute of Physics.* [DOI: 10.1063/1.1759625]

I. INTRODUCTION

Clusters, as aggregates of atoms or molecules that range in size from two to tens of thousands of monomer units, can be viewed as an intermediate state of matter between finite and bulk. Many of the cluster properties, such as structural and thermodynamic, for example, are different from the corresponding bulk properties because of the large number of surface species and finite size effects.

One thermodynamic property of clusters that has received much experimental[1–7] and theoretical[8–30] attention is the "phase transition." Since phase transitions are characteristic of bulk systems, we shall refer to the phase transformations in clusters as phase changes, adopting the language introduced by Berry and co-workers.[8] In a bulk material, the phase transition from solid to liquid occurs at a definite temperature and the heat capacity at that temperature has a sharp (δ-function-like) peak.[5,6] In clusters, the phase change occurs at a range of temperatures, lying between freezing and melting temperatures, and the heat capacity has a broad peak about the transition temperature owing to finite size effects. Between the freezing and melting temperatures an ensemble of clusters coexists in liquidlike and solidlike forms.[9] With some notable exceptions,[7] the melting transition takes place at lower temperatures than the corresponding bulk.[5,6]

In previous work[31] (hereafter referred to as Paper I, we have explored the energy landscape of the selected binary Lennard-Jones clusters of the type $X_{13-n}Y_n$ and examined the effect of adding n Y impurity atoms on the structures of their X_{13-n} core. In the present work, we extend our studies of the given systems into the thermodynamic domain. Thermodynamic properties, such as the total energy, heat capacity, and first derivative of the heat capacity as a function of temperature, are calculated in both the classical and quantum regime. Our goals are to examine the effect of perturbing atoms on the thermodynamic properties of the selected systems and to understand how the complex topology of the potential energy surface affects phase change phenomena. In addition, we examine the importance of quantum contributions to the phase change phenomena in these systems.

From a computational point of view, these clusters are also interesting because of their complex potential energy surface. The double-funnel character of their potential energy surface makes them a particularly challenging case for Monte Carlo simulations.[19,28,32] Therefore, they constitute a good numerical test for measuring the efficiency of Monte Carlo techniques designed to overcome quasiergodicity in both classical[28,32] and quantum[33] simulations.

The remainder of the paper is organized as follows: In Sec. II we give a brief review of the methods and the model potential we employ to calculate the thermodynamic properties for the given systems. In Sec. III we present the results including the total energy, the heat capacity, and the first derivative of the heat capacity as a function of temperature. The phase change behavior is characterized with the help of the probability distribution of isomers as a function of energy. Finally, in Sec. IV we summarize our findings.

II. COMPUTATIONAL METHOD

In the present section, we describe the computational details of our studies involving binary clusters of the form $X_{13-n}Y_n$. We have chosen to study three systems: $X_{12}Y_1$, $X_{11}Y_2$, and $X_{10}Y_3$. The choice of the systems is motivated by the detailed studies of their potential energy surface (PES) and construction of the associated disconnectivity graphs in the companion paper.[31]

A. Interaction potential

The clusters are modeled by the total potential energy

$$V_{\text{tot}}=\sum_{i<j}^{N} V_{LJ}(r_{ij})+\sum_{i=1}^{N} V_c(\mathbf{r_i}), \tag{1}$$

where $V_{LJ}(r_{ij})$, the pairwise Lennard-Jones potential as a function of the distance r_{ij} between atoms i and j, is given by

$$V_{LJ}(r_{ij})=4\epsilon_{ij}\left[\left(\frac{\sigma_{ij}}{r_{ij}}\right)^{12}-\left(\frac{\sigma_{ij}}{r_{ij}}\right)^{6}\right], \tag{2}$$

---

[a] E-mail: dwbravho_sabo@brown.edu

[b] Present address: Department of Chemistry, University of California, Berkeley, California 94720.

and $V_c(\mathbf{r_i})$ is the confining potential

$$V_c(\mathbf{r_i}) = \epsilon \left(\frac{|\mathbf{r_i} - \mathbf{R}_{\mathrm{c.m.}}|}{R_c} \right)^{20}. \tag{3}$$

In Eq. (2), the constants ϵ_{ij} and σ_{ij} are the energy and length-scale parameters for the interaction of particles i and j.

For the binary clusters, we need to specify both the "like" (X-X, Y-Y) as well as the "mixed" (X-Y) interactions. The mixed Lennard-Jones parameters are obtained from the like Lennard-Jones parameters by usual combination rules[34]

$$\sigma_{XY} = \tfrac{1}{2}(\sigma_{XX} + \sigma_{YY}), \tag{4}$$

$$\epsilon_{XY} = \sqrt{\epsilon_{XX}\epsilon_{YY}}. \tag{5}$$

In the present work, we have chosen to examine selected binary Lennard-Jones clusters of the type $X_{13-n}Y_n$ where the impurity atoms are less massive than their core (X) counterparts. Based on our previous work,[31] we have chosen the X atoms to be argon ($\epsilon_{XX} = 119.8\,\mathrm{K}$, $\sigma_{XX} = 3.405\,\text{Å}$, mass $= 39.948$) and Y atoms to be "neonlike." Specifically, we have chosen the ($\sigma = \sigma_{YY}/\sigma_{XX}$, $\epsilon = \epsilon_{YY}/\epsilon_{XX}$) ratios for the impurity atoms to be (0.8,0.6) for $X_{12}Y_1$ and (0.8,0.5) for both $X_{11}Y_2$ and $X_{10}Y_3$, values that produce interesting classes of potential energy surface topologies. The mass of the Y-atom impurity has been taken to be that of neon (20.1797) in all calculations.

In Eq. (3) $\mathbf{r_i}$ and $\mathbf{R}_{\mathrm{c.m.}}$ are the coordinates of the ith atom and the center of mass of the cluster, respectively. The center of mass of the cluster is given by

$$\mathbf{R}_{\mathrm{c.m.}} = \frac{\sum_{i=1}^{N} m_i \mathbf{r_i}}{\sum_{i=1}^{N} m_i}. \tag{6}$$

Finally, R_c is the radius of the confining sphere[35] while ϵ governs the strength of the confining potential. The role of the confining potential $V_c(\mathbf{r_i})$ is to prevent atoms from permanently leaving the cluster since the cluster in vacuum at any finite temperature is metastable with respect to evaporation.

The optimal choice of the parameter R_c for the confining potential has been discussed in recent work.[36] If R_c is taken to be too small, the properties of the system become sensitive to its choice, whereas large values of R_c can result in problems attaining an ergodic simulation. The classical and quantum Monte Carlo simulations presented here have been performed with $R_c = 2\sigma_{XX}$ and $\epsilon = \epsilon_{XX}$. Since the potential energy surfaces of all the systems studied in the present work display a double-funnel character,[31] their thermodynamic properties are calculated with Monte Carlo methods coupled with the parallel tempering technique[28,32,33,37–42] devised to tackle possible ergodicity problems.

B. Classical Monte Carlo simulation

The total energy $\langle E \rangle$, the constant volume heat capacity $\langle C_V \rangle$, and the first derivative of the heat capacity with respect to the temperature $(\partial \langle C_V \rangle / \partial T)_V$ for clusters consisting of N particles are calculated using the standard expressions

$$\langle E \rangle = \frac{3}{2\beta} N + \langle V \rangle, \tag{7}$$

$$\frac{\langle C_V \rangle}{k_B} = \frac{3}{2} N + \beta^2 [\langle V^2 \rangle - \langle V \rangle^2], \tag{8}$$

$$\frac{1}{k_B} \left(\frac{\partial \langle C_V \rangle}{\partial T} \right)_V = -2\beta \langle C_V \rangle + \beta^4 [\langle V^3 \rangle + 2\langle V \rangle^3 - 3\langle V^2 \rangle \langle V \rangle], \tag{9}$$

where k_B is Boltzmann constant, T is the temperature, $\beta = 1/k_B T$, V is the potential energy, and angular brackets denote the canonical averages with respect to the Boltzmann weight $\exp[-\beta V(\mathbf{x})]$.

1. Parallel tempering and sampling strategy

The parallel tempering Monte Carlo simulations are carried out using a total of 48 parallel streams, each running a replica of the system at a different temperature. The streams are independent and uncorrelated sequences of random numbers that can be generated simultaneously on multiple processors. In this paper, we have used the parallel random number generator library called the scalable parallel random number generator (SPRNG).[43,44] Temperatures are generated in the range from $T_{\min}$ to $T_{\max}$ in such a way that they are distributed as the geometric progression[45]

$$T_j = R_T^{1-j} T_{\min}, \quad 1 \leq j \leq M, \tag{10}$$

where

$$R_T = (T_{\min}/T_{\max})^{1/(M-1)}. \tag{11}$$

We have chosen $T_{\min} = 0.2\,\mathrm{K}$, $T_{\max} = 50\,\mathrm{K}$, and $M = 48$. For the range of temperatures $[T_{\min}, T_{\max}] = [0.2, 50]\,\mathrm{K}$, a number of $M = 48$ streams has produced acceptance probabilities for swaps larger than 40% for all streams and for all simulations performed.

Explicitly, the Monte Carlo simulation is conducted as follows. For each stream, a random walk is carried out through configuration space according to the Metropolis algorithm.[46] The basic Monte Carlo step consists of attempted moves of the physical coordinates associated with a given particle. Each attempted move is either accepted or rejected in accord with the Metropolis prescription. The maximum displacements have been adjusted in order to ensure a 40%–60% acceptance ratio in the Monte Carlo moves. The maximum displacements or step sizes are chosen in an analogous manner to the temperatures, to satisfy geometric progression. In other words, the step size at the temperature T_j is

$$s_{\alpha j} = R^{1-j} s_{\alpha,\min}, \tag{12}$$

where

$$R = (s_{\alpha,\min}/s_{\alpha,\max})^{1/(M-1)} \quad (\alpha = x, y, z). \tag{13}$$

The required acceptance ratio between 40% and 60% is achieved for $s_{\alpha,\min} = 0.3$ a.u., $s_{\alpha,\max} = 1.2$ a.u. and $M = 48$.

We define a *pass* as the minimal set of Monte Carlo attempted moves over all particles in the system. Since the clusters of interest are made of 13 atoms, a pass consists of

13 basic steps. We also define a *block* as a set of 10 000 passes. The size of the block is sufficiently large that the block averages of the estimated quantities are independent for all practical purposes. The simulation is divided in two phases: an equilibration phase that consists of 100 blocks and an accumulation phase that consists of 400 blocks per temperature.

An exchange of configurations between streams at adjacent temperatures has been attempted every 25 passes and it has been accepted or rejected according to the parallel tempering logic.[28,32,33,37–42] A stream at any given temperature attempts a swap of configurations with a stream at adjacent lower and higher temperature in succession. Because of this swapping strategy, the streams at minimum and maximum temperatures are involved in swaps only every 50 passes.

All error bars quoted in the current work correspond to two standard deviations. In order to avoid the cluttering of data the error bars have not been shown. The error bars are comparable to the thickness of the lines drawn in the various graphs.

C. Path integral Monte Carlo simulation

For quantum simulations of the heat capacity, we have employed a reweighted Wiener-Fourier path integral (RW-WFPI) method[47,48] and recently developed energy and heat capacity estimators that can be numerically implemented by finite difference schemes.[33,49] Since the methodology is fully described in the cited references in this section we only present their salient features.

The quantum analogs of the total energy $\langle E\rangle$, the constant volume heat capacity $\langle C_V\rangle$, and its first derivative with respect to the temperature $(\partial\langle C_V\rangle/\partial T)_V$ are given with the following expressions:

$$\langle E\rangle=-\frac{1}{Z}\left(\frac{\partial Z}{\partial\beta}\right)_V, \tag{14}$$

$$\frac{\langle C_V\rangle}{k_B}=\frac{\beta^2}{Z}\left(\frac{\partial^2 Z}{\partial\beta^2}\right)_V-\left[\frac{\beta}{Z}\left(\frac{\partial Z}{\partial\beta}\right)_V\right]^2, \tag{15}$$

$$\begin{aligned}\frac{1}{k_B}\left(\frac{\partial\langle C_V\rangle}{\partial T}\right)_V&=-2\beta\langle C_V\rangle-k_B\beta\left\{\frac{\beta^3}{Z}\left(\frac{\partial^3 Z}{\partial\beta^3}\right)_V\right.\\&\quad+2\left[\frac{\beta}{Z}\left(\frac{\partial Z}{\partial\beta}\right)_V\right]^3-3\left[\frac{\beta^2}{Z}\left(\frac{\partial^2 Z}{\partial\beta^2}\right)_V\right]\\&\quad\left.\times\left[\frac{\beta}{Z}\left(\frac{\partial Z}{\partial\beta}\right)_V\right]\right\},\end{aligned} \tag{16}$$

where Z is a partition function of the system. The partition function is an integral of the diagonal density matrix over whole configuration space

$$Z=\int_{\mathbb{R}^{3N}}\rho(\mathbf{x};\beta)d\mathbf{x}. \tag{17}$$

In the random series path-integral representation,[49] the density matrix can be written as follows:

$$\frac{\rho(\mathbf{x};\beta)}{\rho_{\mathrm{fp}}(\beta)}=\int_{\Omega^{3N}}dP[\overline{\mathbf{a}}]\exp\left\{-\beta\int_0^1 V\left[\mathbf{x}+\sigma\sum_{k=1}^{\infty}\mathbf{a}_k\Lambda_k(u)\right]du\right\}, \tag{18}$$

where $\rho_{\mathrm{fp}}(\beta)$ is the density matrix of a free particle [for the ith free particle $\rho_{\mathrm{fp}i}(\beta)=(m_i/2\pi\hbar^2\beta)^{1/2}$], $dP[\overline{\mathbf{a}}]$ is the probability measure, defined on the space Ω^{3N}

$$dP[\overline{\mathbf{a}}]=\prod_{i=1}^{N}dP[\overline{a_i}], \tag{19}$$

with

$$dP[\overline{a_i}]=\prod_{k=1}^{\infty}d\mathbf{a}_{\mathbf{i},\mathbf{k}}\frac{1}{\sqrt{2\pi}}e^{-\mathbf{a}_{\mathbf{i},\mathbf{k}}^2/2}. \tag{20}$$

The vectors $\mathbf{a}_k^T=(\mathbf{a}_{\mathbf{1},k},\mathbf{a}_{\mathbf{2},k},\ldots,\mathbf{a}_{\mathbf{N},k})$ are path variables or independent identically distributed (i.i.d) standard normal variables with $\mathbf{a}_{\mathbf{i},k}=(a_{xi,k},a_{yi,k},a_{zi,k})$. The vector $\mathbf{x}^T=(\mathbf{x}_1,\mathbf{x}_2,\ldots,\mathbf{x}_N)$ represents the physical variables of the system, while σ for the ith particle is $(\hbar^2\beta/m_i)^{1/2}$ where m_i is its mass. $\sigma\mathbf{a}_k$ can be written as

$$\sigma\mathbf{a}_k=\begin{pmatrix}\sigma_1 a_{1,k}\\ \vdots\\ \sigma_N a_{N,k}\end{pmatrix}.$$

The reader should note that $\sigma_i=(\sigma_{xi},\sigma_{yi},\sigma_{zi})$ and $\sigma_{xi}=\sigma_{yi}=\sigma_{zi}$. $\Lambda_k(u)$ are a set of functions defined in the following way. Let $\{\lambda_k(\tau)\}_{k\geqslant 1}$ be a set of functions defined on the interval $[0,1]$ that, together with the constant function $\lambda_0(\tau)=1$, make up an orthonormal basis in $L^2[0,1]$. Then, $\Lambda_k(u)$ is defined as

$$\Lambda_k(u)=\int_0^u\lambda_k(t)dt.$$

In practical applications, the series in Eq. (18) needs to be replaced by a finite sum. Within the RW-WFPI framework, a finite dimensional approximation to the exact density matrix in Eq. (18) is given by the expression

$$\frac{\rho_n(\mathbf{x};\beta)}{\rho_{\mathrm{fp}}(\beta)}=\int_{\Omega^{3N}}dP[\overline{\mathbf{a}}]\exp\left\{-\beta\int_0^1 V\left[\mathbf{x}+\sigma\sum_{k=1}^{4n}\mathbf{a}_k\tilde{\Lambda}_{n,k}(u)\right]du\right\}. \tag{21}$$

The functions,

$$\tilde{\Lambda}_{n,k}(u)=\sqrt{\frac{2}{\pi^2}}\frac{\sin(k\pi u)}{k} \tag{22}$$

for $1\leqslant k\leqslant n$, and

$$\tilde{\Lambda}_{n,k}(u)=f(u)\sin(k\pi u) \tag{23}$$

for $n<k\leqslant 4n$, are chosen so that to maximize the rate of convergence,

$$\rho_n(\mathbf{x};\beta)\to\rho(\mathbf{x};\beta).$$

The function $f(u)$ is defined as[47]

$$f(u)=\left[\frac{u(1-u)-2/\pi^2\Sigma_{k=1}^{n}\sin^2(k\pi u)/k^2}{\Sigma_{k=n+1}^{4n}\sin^2(k\pi u)}\right]^{1/2}.$$

Therefore, a path that starts and ends in the same configuration space $\mathbf{x}$ (called a thermal loop) can be written

$$\mathbf{x}(u)=\mathbf{x}+\sigma\left[\sum_{k=1}^{n}a_k\sqrt{\frac{2}{\pi^2}}\frac{\sin(k\pi u)}{k}\right.$$
$$\left.+f(u)\sum_{k=n+1}^{4n}a_k\sin(k\pi u)\right].$$

It turns out to be useful to define several auxiliary quantities[48]

$$U_n(\mathbf{x},\overline{\mathbf{a}};\beta)=\int_0^1 V[\mathbf{x}(u)]du, \tag{24}$$

$$X_n(\mathbf{x},\overline{\mathbf{a}};\beta)=\rho_{\mathrm{fp}}(\beta)\exp[-\beta U_n(\mathbf{x},\overline{\mathbf{a}};\beta)], \tag{25}$$

and

$$\begin{aligned}R_n(\mathbf{x},\overline{\mathbf{a}};\beta,\epsilon)&=\frac{X_n(\mathbf{x},\overline{\mathbf{a}};\beta\epsilon)}{X_n(\mathbf{x},\overline{\mathbf{a}};\beta)}\\&=\epsilon^{-3N/2}\exp[-\beta\epsilon U_n(\mathbf{x},\overline{\mathbf{a}};\beta\epsilon)\\&\quad+\beta U_n(\mathbf{x},\overline{\mathbf{a}};\beta)].\end{aligned} \tag{26}$$

Then it is easy to show that, for $k=1$, 2, 3, we have

$$\frac{\beta^k}{Z}\left(\frac{\partial^k Z}{\partial\beta^k}\right)_V=\frac{\int_{\mathbb{R}^{3N}}d\mathbf{x}\int_{\Omega^{3N}}dP[\overline{\mathbf{a}}]X_n(\mathbf{x},\overline{\mathbf{a}};\beta)\left.\frac{d^k}{d\epsilon^k}R_n(\mathbf{x},\overline{\mathbf{a}};\beta,\epsilon)\right|_{\epsilon=1}}{\int_{\mathbb{R}^{3N}}d\mathbf{x}\int_{\Omega^{3N}}dP[\overline{\mathbf{a}}]X_n(\mathbf{x},\overline{\mathbf{a}};\beta)}. \tag{27}$$

The quantities above can be evaluated by Monte Carlo integration, where the canonical averages are carried out with respect to the Boltzmann-like weight $\exp[-\Sigma_{i=1}^{N}\Sigma_{k=1}^{4n}\mathbf{a}_{\mathbf{i,k}}^2/2-\beta U_n(\mathbf{x},\overline{\mathbf{a}};\beta)]$. The derivatives of the quantity $R_n(\mathbf{x},\overline{\mathbf{a}};\beta)$ can be expressed in terms of the derivatives of the quantity $U_n(\mathbf{x},\overline{\mathbf{a}};\beta)$

$$\left.\frac{d}{d\epsilon}R_n(\mathbf{x},\overline{\mathbf{a}};\beta,\epsilon)\right|_{\epsilon=1}=-\frac{3N}{2}-\beta U_n(\mathbf{x},\overline{\mathbf{a}};\beta)-\beta\left.\frac{d}{d\epsilon}U_n(\mathbf{x},\overline{\mathbf{a}};\beta\epsilon)\right|_{\epsilon=1}, \tag{28}$$

$$\left.\frac{d^2}{d\epsilon^2}R_n(\mathbf{x},\overline{\mathbf{a}};\beta,\epsilon)\right|_{\epsilon=1}=\left[\left.\frac{d}{d\epsilon}R_n(\mathbf{x},\overline{\mathbf{a}};\beta,\epsilon)\right|_{\epsilon=1}\right]^2+\frac{3N}{2}-2\beta\left.\frac{d}{d\epsilon}U_n(\mathbf{x},\overline{\mathbf{a}};\beta\epsilon)\right|_{\epsilon=1}-\beta\left.\frac{d^2}{d\epsilon^2}U_n(\mathbf{x},\overline{\mathbf{a}};\beta\epsilon)\right|_{\epsilon=1}, \tag{29}$$

and

$$\begin{aligned}\left.\frac{d^3}{d\epsilon^3}R_n(\mathbf{x},\overline{\mathbf{a}};\beta,\epsilon)\right|_{\epsilon=1}&=\left[\left.\frac{d}{d\epsilon}R_n(\mathbf{x},\overline{\mathbf{a}};\beta,\epsilon)\right|_{\epsilon=1}\right]^3+3\left[\left.\frac{d}{d\epsilon}R_n(\mathbf{x},\overline{\mathbf{a}};\beta,\epsilon)\right|_{\epsilon=1}\right]\left[\frac{3N}{2}-2\beta\left.\frac{d}{d\epsilon}U_n(\mathbf{x},\overline{\mathbf{a}};\beta\epsilon)\right|_{\epsilon=1}\right.\\&\quad\left.-\beta\left.\frac{d^2}{d\epsilon^2}U_n(\mathbf{x},\overline{\mathbf{a}};\beta\epsilon)\right|_{\epsilon=1}\right]+\left[\frac{3N}{2}-2\beta\left.\frac{d}{d\epsilon}U_n(\mathbf{x},\overline{\mathbf{a}};\beta\epsilon)\right|_{\epsilon=1}-\beta\left.\frac{d^2}{d\epsilon^2}U_n(\mathbf{x},\overline{\mathbf{a}};\beta\epsilon)\right|_{\epsilon=1}\right]\\&\quad-\left[3N+3\beta\left.\frac{d^2}{d\epsilon^2}U_n(\mathbf{x},\overline{\mathbf{a}};\beta\epsilon)\right|_{\epsilon=1}+\beta\left.\frac{d^3}{d\epsilon^3}U_n(\mathbf{x},\overline{\mathbf{a}};\beta\epsilon)\right|_{\epsilon=1}\right].\end{aligned} \tag{30}$$

The derivatives with respect to ϵ are evaluated numerically by a finite difference approximation

$$\begin{aligned}\left.\frac{d}{d\epsilon}U_n[\mathbf{x},\overline{\mathbf{a}};\beta\epsilon]\right|_{\epsilon=1}&\approx(2\epsilon_0)^{-1}\times\{U_n[\mathbf{x},\overline{\mathbf{a}};\beta(1+\epsilon_0)]\\&\quad-U_n[\mathbf{x},\overline{\mathbf{a}};\beta(1-\epsilon_0)]\},\end{aligned} \tag{31}$$

$$\begin{aligned}\left.\frac{d^2}{d\epsilon^2}U_n(\mathbf{x},\overline{\mathbf{a}};\beta\epsilon)\right|_{\epsilon=1}&\approx\epsilon_0^{-2}\{U_n[\mathbf{x},\overline{\mathbf{a}};\beta(1+\epsilon_0)]\\&\quad-2U_n[\mathbf{x},\overline{\mathbf{a}};\beta]+U_n[\mathbf{x},\overline{\mathbf{a}};\beta(1-\epsilon_0)]\},\end{aligned} \tag{32}$$

and

$$\begin{aligned}\frac{d^3}{d\epsilon^3}U_n(\mathbf{x},\overline{\mathbf{a}};\beta\epsilon)|_{\epsilon=1}&\approx\epsilon_0^{-3}\{U_n[\mathbf{x},\overline{\mathbf{a}};\beta(1+2\epsilon_0)]\\&\quad-3U_n[\mathbf{x},\overline{\mathbf{a}};\beta(1+\epsilon_0)]\\&\quad+3U_n[\mathbf{x},\overline{\mathbf{a}};\beta]\\&\quad-U_n[\mathbf{x},\overline{\mathbf{a}};\beta(1-\epsilon_0)]\}.\end{aligned} \tag{33}$$

1. Parallel tempering and sampling strategy

The sampling strategy is similar to the one employed in the classical Monte Carlo simulations. Here, with each attempted move of the physical coordinate $\mathbf{x}_i$ of a particle, we attempt to move a randomly selected path variable associated with that particle. A *pass* is defined as the minimal set of Monte Carlo attempted moves over all 13 particles in the system. We define a block as a set of 10 000 passes. Exceptions are simulations with 32 and 64 path variables, where a block contains 20 000 passes. For each simulation 400 blocks have been utilized.

The maximum displacements for the physical coordinates are chosen analogously to those utilized in classical simulations [see Eqs. (12) and (13)], while the maximum displacements for the path variables are chosen in the following way: $\Delta_{kj}=As_{xj}$ at temperature T_j, where A is a constant chosen so that the acceptance ratio for each randomly selected path variable is between 40% and 60%.

We implement a parallel tempering procedure that is analogous to the one utilized in classical simulations. An exchange of configurations between streams at adjacent temperatures has been attempted every 25 passes and it has been accepted or rejected according to the parallel tempering prescription. By monitoring the acceptance ratios for all 48 streams we have found that values have been larger than 40% for all simulations performed. It should be noted that the exchange of configurations between streams includes both particle (physical) coordinates as well as their associated path variables.

The value of the discretization step ϵ_0 needed to evaluate a finite difference approximation to the derivatives with respect to ϵ has been set to $\epsilon_0=2^{-12}$. The order of error for the third derivative is $O(\epsilon_0)$ while for the first and the second derivative it is $O(\epsilon_0^2)$. We would like to mention that the error introduced in the evaluation of the first derivative of the heat capacity (total energy, heat capacity), from the finite difference approximation, is at least 10 (1000) times smaller than the corresponding statistical error for all simulations performed.

We end this section with a comment on the convergence and the error bars involved in the determination of the total energy and the heat capacity. The convergence of the total energy and the heat capacity has been tested with respect to the number of path variables. We have found the results to be converged for $4n=32$ path variables. Further increasing the number of path variables to 64 has yielded the same results within the statistical error (two standard deviations). The error bars have not been shown in the graphs in order to avoid the cluttering of data. For all but the lowest temperatures the error bars are comparable to the thickness of the lines displayed in the graphs. For reference, at the lowest temperature at which the path integral simulations have been performed, $T=4$ K, the following results have been obtained for $X_{10}Y_3$: $\langle E\rangle=-296.47\pm0.13$, $\langle C_V\rangle/Nk_B=0.52\pm0.20$, $(\partial\langle C_V\rangle/\partial T)_V/Nk_B=-0.10\pm0.54$. For the same system but at the temperature 7.22 K we have obtained the following: $\langle E\rangle=-293.74\pm0.07$, $\langle C_V\rangle/Nk_B=1.10\pm0.04$, $(\partial\langle C_V\rangle/\partial T)_V/Nk_B=0.15\pm0.06$.

D. Quenching procedure

We have performed minimization or quenching of the parallel tempering Monte Carlo (classical and quantum) sampled configurations by implementing the Fletcher-Reeves-Polak-Ribiere version of the conjugate gradient method using the algorithm given in *Numerical Recipes*.[50] The quenches allow us to interpret structural transformations in the clusters that are associated with the peaks in the heat capacity curves as well as variations in the slopes of the caloric and the first derivative of the heat capacity curves.

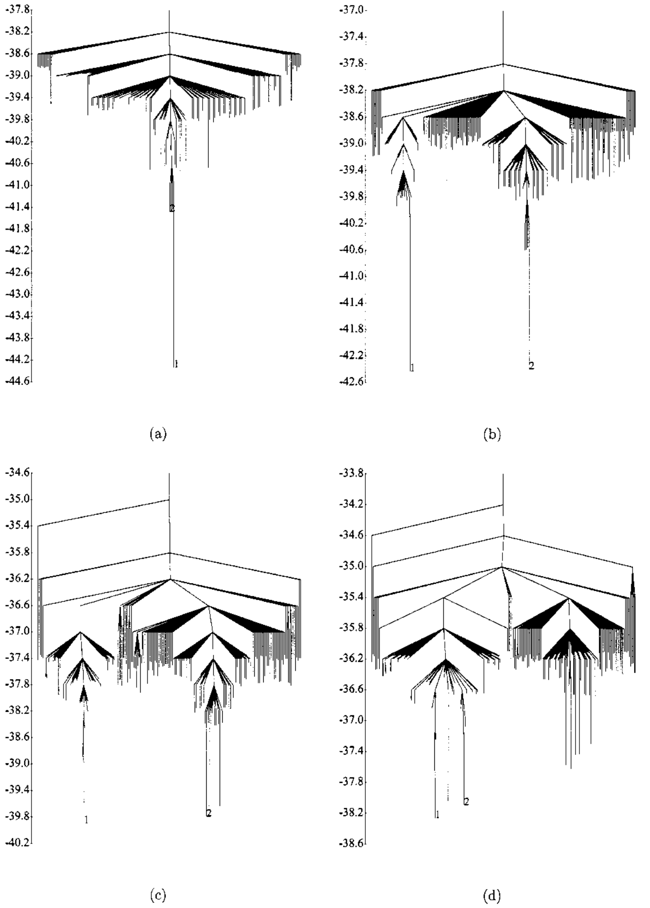

FIG. 1. Disconnectivity graph for (a) X_{13}, (b) $X_{12}Y_1$, (c) $X_{11}Y_2$, and (d) $X_{10}Y_3$. The energy scale is in units of ϵ_{XX}. The (σ,ϵ) values for panels (a)–(d) are (1.0,1.0), (0.8,0.6), (0.8,0.5), and (0.8,0.5), respectively. Only branches leading to the 200 lowest-energy minima are shown.

III. RESULTS AND DISCUSSION

In this section, we present the results of classical and quantum parallel tempering Monte Carlo simulations performed on each of the $X_{12}Y_1$, $X_{11}Y_2$ and $X_{10}Y_3$ clusters. The details about the calculations are given in Sec. II.

Figure 1 shows disconnectivity graphs for the studied system together with a disconnectivity graph for the homogeneous X_{13} cluster. A description of the construction of a disconnectivity graph is given in the companion paper[31] and references therein. A disconnectivity graph is a useful tool for the visualization of the underlying potential energy surface of the studied systems.[51,52]

While the potential energy surface of the homogeneous X_{13} cluster is characterized by a single funnel,[53] those for $X_{12}Y_1$, $X_{11}Y_2$, and $X_{10}Y_3$ have a double-funnel structure. The global minimum of each system is labeled by the num-

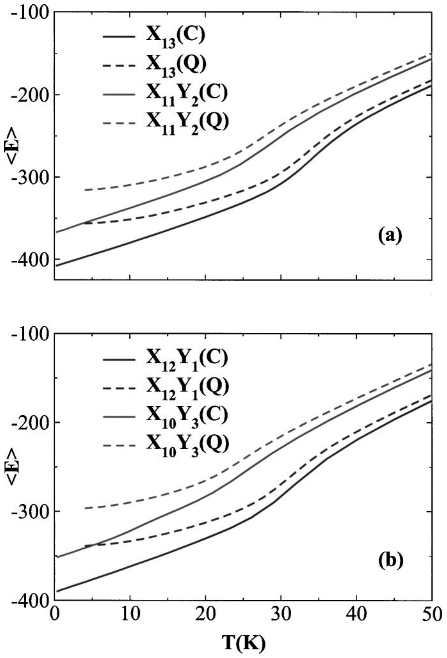

FIG. 2. Classical and quantum caloric curves for the studied systems. Solid (dashed) lines represent classical-C (quantum-Q) results. $\langle E\rangle$ is given in units of kelvin per particle. The number of path variables employed in the path integral simulations is $4n=32$.

ber 1 and the next higher-lying inherent structure is labeled by the number 2. For the $X_{12}Y_1\,[X_{11}Y_2]$ cluster, inherent structures $1\,(E=-42.426\epsilon_{XX})\,[(E=-39.891\epsilon_{XX})]$ and $2\,(E=-42.392\epsilon_{XX})\,[(E=-39.787\epsilon_{XX})]$ define two basins of similar energies separated by a large energy barrier. For the $X_{10}Y_3$ cluster, two basins are associated with inherent structure $1\,(E=-38.257\epsilon_{XX})$ (inherent structures 2 and 3 belong to the basin defined by inherent structure 1) and inherent structure $4\,(E=-37.618\epsilon_{XX})$. The lowest energy basin of the $X_{12}Y_1$ cluster contains 30 inherent structures compared with 67 inherent structures in the basin associated with the second lowest minimum, inherent structure 2. Two distinct funnels on the PES of $X_{11}Y_2$ cluster, one associated with inherent structure 1 and another with inherent structure 2, contain 56 and 116 inherent structures, respectively. Therefore, their lowest energy basin is slightly narrower than the second basin. On the other hand, two funnels on the PES of the $X_{10}Y_3$ cluster, one associated with inherent structure 1 and another with inherent structure 4, contain 98 and 85 minima, respectively. The number of inherent structures associated with a basin often indicates the likelihood that the system will relax to the minimum at the bottom of that basin.

Figure 2 displays the caloric curves, i.e., the average total energy of the clusters, as a function of temperature. Solid lines represent classical results, while dashed lines represent quantum results. The caloric curves of the homogeneous X_{13} cluster are included for comparison purposes. Comparison of the classical and quantum caloric curves indicates that quantum effects are considerable over the entire temperature range. A variation in the slope of the caloric curves is characteristic of a phase change in the clusters.

The constant volume heat capacity curves of the studied clusters as a function of temperature obtained by classical and quantum simulations are shown in Figs. 3 and 4, respectively. Again, the results for the X_{13} cluster are shown for comparison. Replacement of n X (Ar) atoms in the homogeneous clusters by n Y (Ne) atoms manifests itself in Fig. 3 in such a way that the maxima of the heat capacity curves are shifted toward lower temperatures with respect to the maximum of the heat capacity of the homogeneous cluster. A similar trend is seen for the quantum heat capacities (see Fig. 4). From Fig. 3, it can be seen that binary clusters exhibit lower temperature peaks, in addition to higher temperature peaks. Their numerical values and temperatures at which they occur are listed in Table I. Both higher and lower temperature maxima are to be discussed in more details in sections below. As can be seen from Fig. 4, lower temperature peaks are absent from the heat capacity curves obtained by path integral simulations, at least in the temperature range (from 4 to 50 K) considered here. Numerical values of the quantum heat capacity peaks with associated temperatures are listed in Table II.

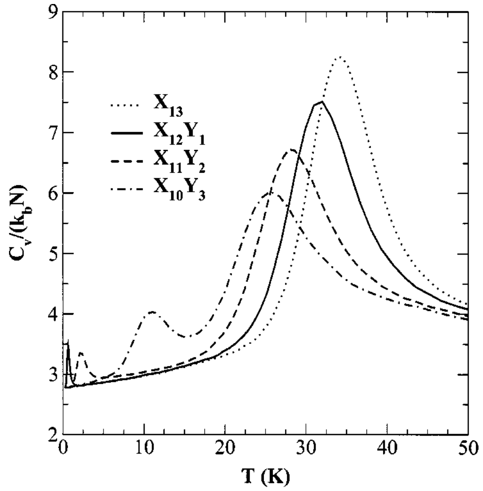

FIG. 3. Classical heat capacities per particle for studied systems in units of k_B as a function of temperature.

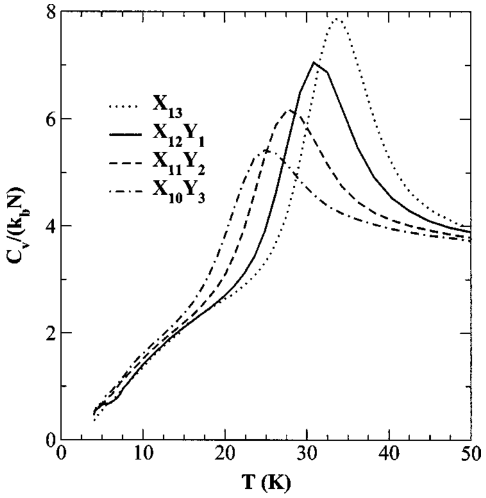

FIG. 4. Quantum heat capacities per particle for studied systems in units of k_B as a function of temperature. The number of path variables employed in the simulations is $4n=32$.

TABLE I. Classical heat capacity peak parameters for 13 atom clusters. The temperature is given in kelvin while the heat capacity is given in units of k_B per particle. The values are obtained by a cubic spline interpolation of the parallel tempering data shown in Fig. 3. The heat capacity error bars estimates are averages of two standard deviations of the points near the peaks.

	Lower temperature peak		Higher temperature peak	
	T_{peak}	$\langle C_V \rangle / k_b N$	T_{peak}	$\langle C_V \rangle / k_b N$
X_{13}			34.09±0.18	8.27±0.06
$X_{12}Y_1$	0.65±0.01	3.48±0.02	31.67±0.08	7.54±0.05
$X_{11}Y_2$	2.21±0.07	3.36±0.02	28.18±0.24	6.73±0.04
$X_{10}Y_3$	11.09±0.17	4.03±0.02	25.61±0.05	6.03±0.04

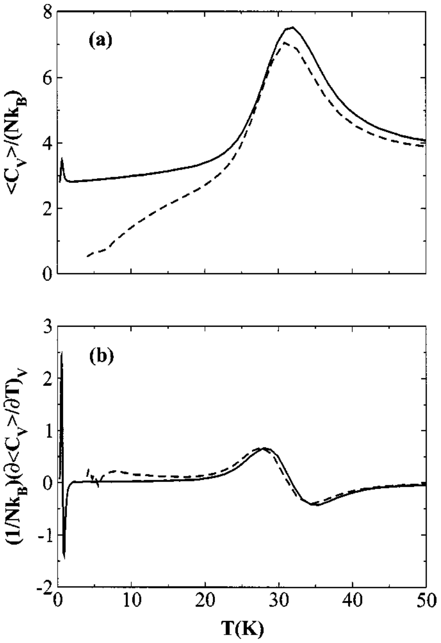

FIG. 5. $X_{12}Y_1$. Panel (a) shows classical (solid line) and quantum (dashed line)-heat capacities per particle in units of k_B as a function of temperature. Panel (b) shows first derivative of the heat capacity per particle in units of k_B. The solid (dashed) line represents classical (quantum) results. The number of path variables employed in the path integral simulations is $4n=32$.

A. $X_{12}Y_1$

The heat capacity curves and their first derivatives obtained by classical and path integral Monte Carlo simulations are shown in Figs. 5(a) and 5(b), respectively. The solid lines are classical results.

1. Classical simulation

The heat capacity has a broad peak at a temperature of about 31.7 K and a narrow, low temperature peak at about 0.65 K. In order to identify the phase changes associated with the peaks in the heat capacity curves, the configurations generated by parallel tempering Monte Carlo simulations at a temperature somewhat below and above the temperatures of the peaks in the heat capacity curves have been quenched. The results of the quenches are shown in Fig. 6. Quenching from the configurations sampled at 0.3 K yields only inherent structure 1 (global minimum-Y atom is in the interior of the cluster; center of the icosahedron). The quenches of the configurations sampled at 1.7 K produce predominantly inherent structure 2 (Y atom is on the surface of the cluster), although there is still a small population (0.06) of inherent structure 1. The low temperature peak in the classical heat capacity curve is associated with the structural transition from inherent structure 1 to inherent structure 2, that is, a solid ↔ solid phase change between two basins (see Fig. 6).

The high probability (≈0.94) of finding the $X_{12}Y_1$ cluster to "dwell" in inherent structure 2, at a very low temperature of 1.7 K might be surprising at first sight. One possible explanation is likely to be found in the shape of its disconnectivity graph, see Fig. 1(b). As we noticed earlier, by examining its disconnectivity graph, the energy landscape displays a double-funnel structure. The funnel associated with inherent structure 2 contains twice as many local minima as the funnel associated with inherent structure 1. Even though funnel 1 is energetically more favorable, owing to the larger

TABLE II. Quantum heat capacity peak parameters for 13 atom clusters. The temperature is given in kelvin while the heat capacity is given in units of k_B per particle. The values are obtained by a cubic spline interpolation of the parallel tempering data shown in Fig. 4. The number of path variables employed in the quantum calculations is $4n=32$. The heat capacity error bars estimates are averages of two standard deviations of the points near the peaks.

	Lower temperature peak		Higher temperature peak	
	T_{peak}	$\langle C_V \rangle / k_b N$	T_{peak}	$\langle C_V \rangle / k_b N$
X_{13}			33.68±0.21	7.89±0.04
$X_{12}Y_1$			31.23±0.27	7.07±0.04
$X_{11}Y_2$			27.88±0.30	6.16±0.04
$X_{10}Y_3$			24.86±0.12	5.42±0.03

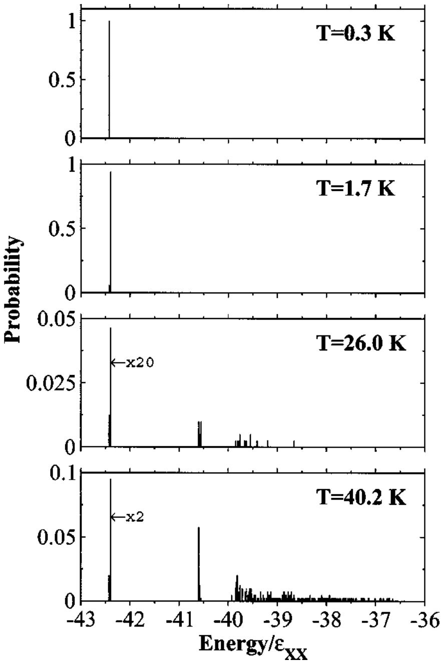

FIG. 6. Distributions of the inherent structures for the $X_{12}Y_1$ cluster, generated by quenching configurations sampled from classical parallel tempering Monte Carlo simulations at temperatures above and below the solid ↔ solid transition (1.7 and 0.3 K) and above and below the solid ↔ liquid transition (40.2 and 26.0 K). Note that the lines representing the population of inherent structure 2 at energy $-42.392\epsilon_{XX}$, labeled "×20" and "×2", have been reduced by a factor of 20 and 2, respectively.

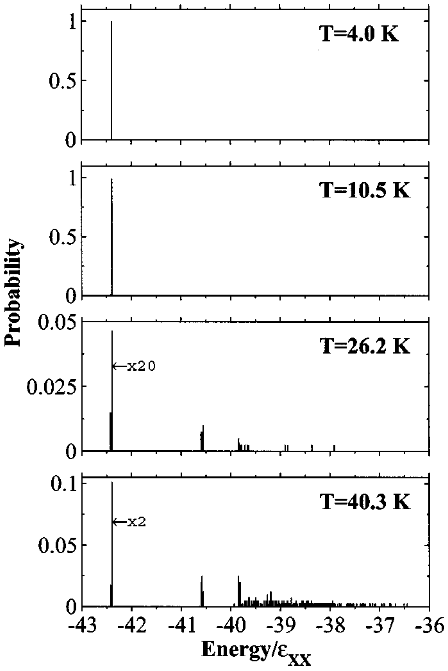

FIG. 7. Distributions of the inherent structures for the $X_{12}Y_1$ cluster, generated by quenching configurations sampled from quantum parallel tempering Monte Carlo simulations at temperatures 4 K, 10.5 K, and temperatures below (26.2 K) and above (40.3 K) the solid ↔ liquid transition. Note that the lines representing the population of inherent structure 2 at energy $-42.392\epsilon_{XX}$, labeled "×20" and "×2", have been reduced by a factor of 20 and 2, respectively.

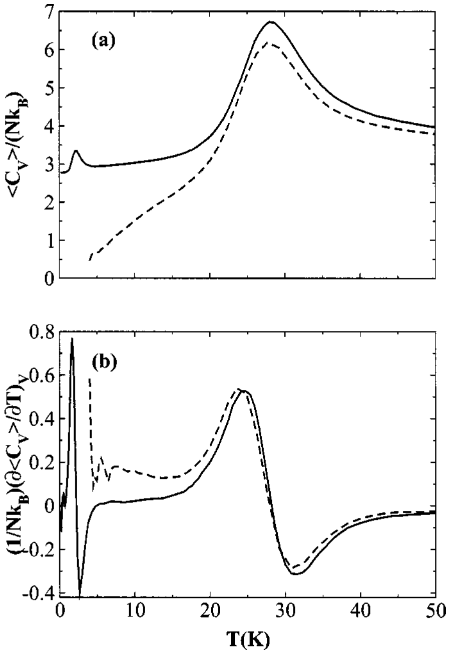

FIG. 8. $X_{11}Y_2$. Panel (a) shows classical (solid line) and quantum (dashed line) heat capacities per particle in units of k_B as a function of temperature. Panel (b) shows the first derivative of the heat capacity per particle in units of k_B. The solid (dashed) line represents classical (quantum) results. The number of path variables employed in the path integral simulations is $4n=32$.

number of minima associated with funnel 2, the volume of the configuration space available to funnel 2 is likely to be larger than the one available to funnel 1 and makes it entropicaly more favorable. However, it should be noted that the number of minima in a disconnectivity graph does not necessarily indicate the volume of available configuration space. Another possible explanation is that inherent structure 1 has a smaller vibrational entropy.[54] At a temperature $T=26\,\mathrm{K}$ (below the T_{peak}) the system occupies mainly (≈0.93) inherent structure 2. However, a very small population of inherent structure 1 and higher energy amorphous structures is present. As the temperature increases, the population of higher energy amorphous structures rapidly increases and at $T=40.2\,\mathrm{K}$ they begin to dominate. Thus, the broad peak in the heat capacity at $T=31.67\,\mathrm{K}$ is associated with the solid↔liquid phase change.

2. Path integral simulation

Unlike the classical heat capacity, the quantum heat capacity curve has only one peak, centered near $T=31.23\,\mathrm{K}$. It can be seen from Fig. 5 and by comparing the numerical results from Tables I and II that the solid-liquid phase change in the "quantum" system occurs at slightly lower temperature than in the "classical" one. Quantum effects lower the transition temperature by 1.4%. Likewise, there is a decrease in the height of the heat capacity maximum. The lowering of the transition temperature and the height of the heat capacity peak from quantum effects are expected and have been documented in the literature.[10,25,30,55] These phenomena are the consequence of the zero-point motion and/or tunneling that effectively raise the energy of the inherent structures, lower the energy barriers between them, and thus allow for easier isomerization.

From the distribution of inherent structures at $T=4\,\mathrm{K}$ (see Fig. 7) it can be seen that the system "likes" to stay in inherent structure 2 with the probability 1.0. A normal mode analysis of inherent structures 1 and 2 shows that estimated zero-point energy of inherent structure 1 lies about 22 cm^{-1} higher than the corresponding zero-point energy associated with inherent structure 2. At the temperature of 10.5 K, there is still a very high population (≈0.99) of inherent structure 2 with almost a negligible population of inherent structure 1 (≈0.01). We have compared the classical distribution of inherent structures at approximately the same temperatures ($T=4.09\,\mathrm{K}$ and $T=10.9\,\mathrm{K}$) with its quantum counterpart. It has been found that the global minimum in the classical case is slightly more likely to be populated than in the quantum case. At the temperatures below (26.2 K) and above (40.3 K) the temperature at which the solid↔liquid phase change occurs, the classical and quantum distributions of inherent structures are similar.

B. $X_{11}Y_2$

The heat capacity curves and their first derivatives obtained by classical and path integral Monte Carlo simulations are shown in Figs. 8(a) and 8(b), respectively. The solid lines are classical results.

1. Classical simulation

As is the case with $X_{12}Y_1$, the heat capacity curve of the $X_{11}Y_2$ cluster has two peaks. A broad, high temperature peak

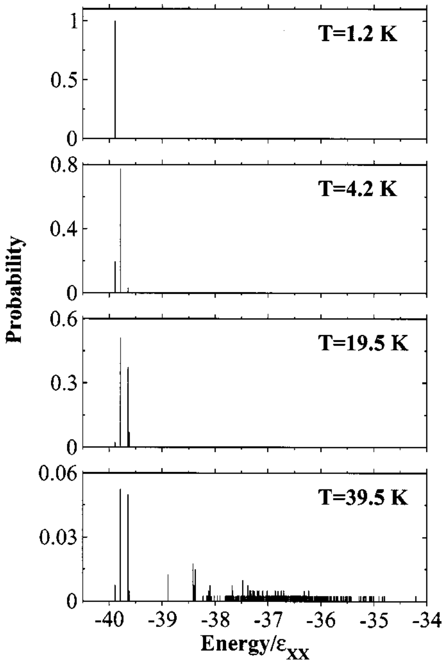

FIG. 9. Distributions of the inherent structures for the $X_{11}Y_2$ cluster, generated by quenching configurations sampled from classical parallel tempering Monte Carlo simulations at temperatures above and below the solid↔solid transition (4.2 and 1.2 K) and above and below the solid↔liquid transition (39.5 and 19.5 K).

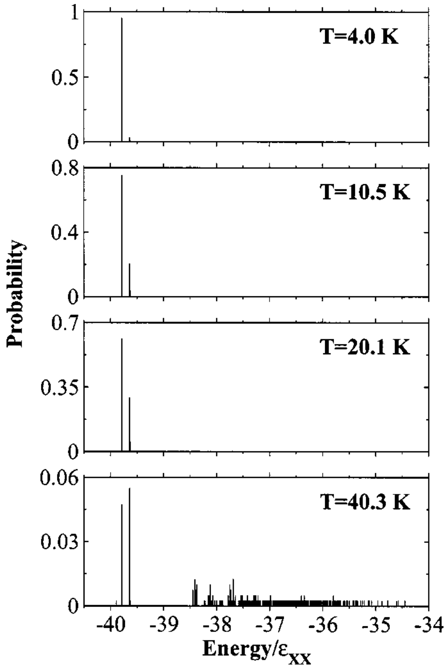

FIG. 10. Distributions of the inherent structures for the $X_{11}Y_2$ cluster, generated by quenching configurations sampled from quantum parallel tempering Monte Carlo simulations at temperatures 4 K, 10.5 K, and temperatures below (20.1 K) and above (40.3 K) the solid↔liquid transition.

occurs at 28.18 K and a smaller, narrower peak occurs at 2.21 K. Quenching of the configurations generated at $T = 1.2$ K gives only inherent structure 1 (one Y atom is in the interior and the other is on the surface of the cluster). The quenches of the configurations generated at $T = 4.2$ K yield inherent structures 1, 2, and 3 with the population probability of approximately 0.2, 0.77, and 0.03, respectively. Inherent structures 2 and 3 belong to the same funnel. Thus, the low temperature peak in the heat capacity curve is associated with the structural transition between inherent structure 1 and inherent structure 2 and corresponds to a solid↔solid phase change.

The high probability of occupying inherent structure 2 at a relatively low temperature could be explained in an analogous manner to that for the $X_{12}Y_1$ cluster. The funnel associated with inherent structure 2 [see Fig. 1(b)] contains two times more minima than the one associated with inherent structure 1 and is likely to have a larger entropy.

At a temperature $T = 19.5$ K, inherent structures 2, 3, and 4 associated with funnel 2 dominate in the quench distribution. There is also a very small population of the amorphous (glassy) structures. At $T = 39.5$ K, which is on the high temperature side of the higher peak in the heat capacity curve, the inherent structures from the basin 2 still dominate, but there is an appreciable population of the higher energy amorphous structures. This indicates that the cluster undergoes a phase change from a solidlike to a liquidlike form (see Fig. 9).

2. Path integral simulation

In the temperature range examined in this work, the quantum heat capacity curve has only one peak at $T = 27.88$ K. From Fig. 8 one can see that the quantum effects affect the phase change in the $X_{11}Y_2$ cluster by shifting the solid-liquid transition temperature toward lower temperatures and decreasing the height of the maximum of the heat capacity curve. The change in the transition temperature with respect to the classical result is approximately 1.1%.

The quenches from the configurations sampled by quantum parallel tempering Monte Carlo simulations at 4 K yield inherent structures 2, 3, and 4 (associated with the basin 2) with the probability 0.95, 0.04, and 0.01, respectively. There is no measurable population of the global minimum at that temperature. Comparing the quantum distribution (see Fig. 10) of the inherent structures at 4 K with the classical distribution (see Fig. 9) at approximately the same temperature, $T = 4.2$ K, we see that there is a sizable population of the global minimum in the classical results. Why is that? An explanation is in the quantum effects, i.e., zero-point energy. We have performed a normal mode analysis of inherent structures 1 and 2 and have found that the estimate of zero-point energy of inherent structure 1 lies about 30 cm^{-1} higher than the corresponding zero-point energy associated with inherent structure 2. At $T = 10.5$ K, the quenching again yields inherent structures 2, 3, and 4 but with probability 0.75, 0.21, and 0.04, respectively. At the temperatures below (20.1 K) and above (40.3 K) the temperature at which the solid↔liquid phase change occurs, the classical and quantum distributions of the inherent structures are similar.

C. $X_{10}Y_3$

The heat capacity curves and their first derivatives obtained by classical and path integral Monte Carlo simulations are shown in Figs. 11(a) and 11(b), respectively. The solid lines are classical results.

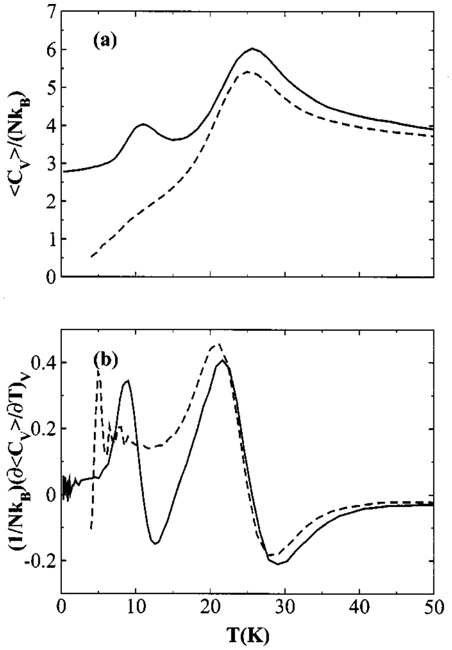

FIG. 11. $X_{10}Y_3$. Panel (a) shows classical (solid line) and quantum (dashed line) heat capacities per particle in units of k_B as a function of temperature. Panel (b) shows the first derivative of the heat capacity per particle in units of k_B. The solid (dashed) line represents classical (quantum) results. The number of path variables employed in the path integral simulations is $4n=32$.

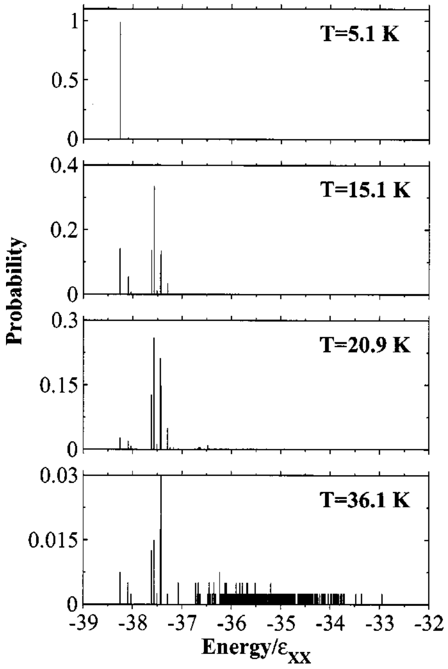

FIG. 12. Distributions of the inherent structures for the $X_{10}Y_3$ cluster, generated by quenching configurations sampled from classical parallel tempering Monte Carlo simulations at temperatures above and below the solid↔solid transition (15.1 and 5.1 K) and above and below the solid↔liquid transition (36.1 and 20.9 K).

1. Classical simulation

The heat capacity has a broad peak at a temperature of about 25.6 K and a narrower, low temperature peak at about 11.1 K Quenching of the configurations generated at 5.1 K (see Fig. 12) obtains inherent structures 1 and 2 with probabilities of 0.99 and 0.01, respectively. Both inherent structures 1 and 2 belong to the funnel associated with inherent structure 1. At the temperature 15.1 K, the quenches of the sampled configurations obtain two groups of inherent structures. One group, comprised of the low-lying inherent structures (1, 2, 3, and 6), belongs to the funnel associated with inherent structure 1 and the other group, comprised of the low-lying inherent structures (4, 5, 7, 8, and 9), belongs to the funnel associated with inherent structure 4. The population probability of the low-lying inherent structures at the bottom of the funnel associated with inherent structure 1 is 0.22 while for those structures that belong to the funnel associated with inherent structure 4, the population probability is 0.77. There is also a very small population of the higher-energy, glassylike structures. The low temperature heat capacity peak can be characterized as a phase change arising from the structural transition between two groups of the inherent structures rather than the structural transition between individual inherent structures, which is the case for the $X_{12}Y_1$ and $X_{11}Y_2$ clusters. Therefore, it is characterized as a solid↔solid phase change. As noticed earlier, the energy landscape of $X_{10}Y_3$ has two funnels with approximately the same number of associated inherent structures. As a consequence, it is equally likely that the system upon cooling enters either of the funnels. At the relatively low temperature of 5.1 K the system dwells in the funnel associated with the global minimum, which is not the case for the $X_{12}Y_1$ and $X_{11}Y_2$ clusters as discussed earlier.

At $T=20.9$ K, the group of inherent structures that belongs to the funnel associated with inherent structure 4 dominates in the quench distribution. However, there is a large number of amorphous structures that start to be populated. At $T=36.1$ K the population of amorphous structures rapidly increases. The heat capacity peak at $T=25.61$ K is, therefore, associated with the solid↔liquid phase change (see Fig. 12).

2. Path integral simulation

Unlike the classical heat capacity, in the range of temperatures examined in the current work, the quantum heat capacity curve has only one peak, at the temperature of 24.86 K. This single peak behavior can be seen from Fig. 11 and by comparing the numerical results from Tables I and II that the quantum effects lower the transition temperature by 2.9% with respect to the classical result.

The quenches from the configurations sampled at 5.0 K yield two groups of inherent structures with approximately the same probability (see Fig. 13). Group 1 contains inherent structures 1 and 2, and they belong to the funnel associated with inherent structure 1. Group 2 is made up of inherent structures 4, 5, 7, and 8, and they belong to the funnel associated with inherent structure 4. Comparing the quantum distribution of the inherent structures with its classical counterpart at the same temperature, one can see that quantum effects allow for an easier isomerization between two funnels. Moreover, the quantum effects eliminate the low temperature peak in the quantum

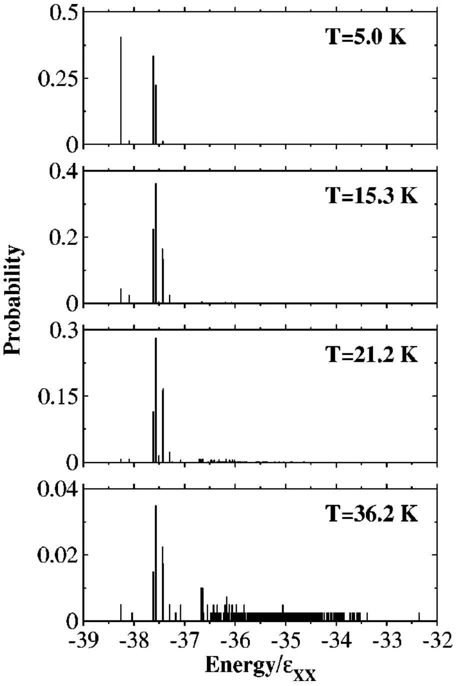

FIG. 13. Distributions of the inherent structures for the $X_{10}Y_3$ cluster, generated by quenching configurations sampled from quantum parallel tempering Monte Carlo simulations at temperatures 5 K, 15.3 K, and temperatures below (21.2 K) and above (36.2 K) the solid↔liquid transition.

heat capacity curve over the studied temperature range. We have also performed a normal mode analysis for $X_{10}Y_3$ and found that the zero-point energy changes the energetic ordering. The zero-point energy of inherent structure 4 lies about 8 cm^{-1} lower than the corresponding zero-point energy associated with inherent structure 1. A similar reversal of the energetic ordering has been found in the $X_{12}Y_1$ and $X_{11}Y_2$ systems and might be a reason for the absence of the low temperature peaks. Another possibility could be that the quantum transitions are shifted to lower temperatures than those studied in the current work. At $T=15.3\,\mathrm{K}$ two groups of inherent structures, group 1 and 2, dominate in the quench distribution. When compared to the classical distribution of inherent structures at approximately the same temperature, one can see that the population probability of group 1 is smaller than in the classical case. At the higher temperatures, the classical and quantum distributions of the inherent structures become similar and amorphous structures dominate. As expected, the heat capacity peak at $T=24.86\,\mathrm{K}$ is associated with the solid↔liquid phase change.

IV. CONCLUSIONS

In this work, we have investigated the melting behavior of the selected binary Lennard-Jones clusters of the form $X_{13-n}Y_n$ [$X_{12}Y_1$ (σ=0.8, ϵ=0.6), $X_{11}Y_2$ (σ=0.8, ϵ=0.5), $X_{10}Y_3$ (σ=0.8, ϵ=0.5)] in both classical and quantum regimes. For the classical results, the total energy, the heat capacity, and the first derivative of the heat capacity are obtained by employing a classical Monte Carlo method in conjunction with parallel tempering, while their quantum counterparts are obtained by employing the path integral (RWFPI) Monte Carlo method combined with parallel tempering. Quenching of the Monte Carlo sampled configurations permits us to identify the structural transitions associated with the peaks in the heat capacity curves.

Classical results show that all three studied systems exhibit a low temperature peak in the heat capacity curve. These low temperature peaks result from a structural transformation between two solidlike low lying, close in energy, inherent structures, or groups of inherent structures. In other words, low temperature peaks are a direct consequence of the double-funnel structure of the underlying potential energy surface of the system. The high temperature peaks are associated with a solid to liquid melting transition.

Replacing n X (core) atoms in the homogeneous cluster with n lighter impurity atoms Y results in the lowering of the melting temperature and the height of the peak of the classical heat capacity when compared to the same quantities in the homogeneous cluster (see Fig. 3). The quantum heat capacity shows a similar trend (see Fig. 4). On the other hand, low temperature peaks in the classical heat capacity curves are shifted toward higher temperatures as the number of atoms Y increases in the clusters.

Quantum effects are important but relatively modest in the whole range of temperatures except in the low temperature regime where they are more pronounced. This is understandable because the dominant species in the clusters are X atoms that mimic (heavier) Ar atoms. As the number of the Y atoms, that mimic (lighter) Ne atoms, increases so does the magnitude of the quantum effect. In general, the magnitude of the quantum effects depends on the particle mass, the temperature, and the relative strengths of the similar and mixed pair interaction potential. Quantum effects do lower the melting temperatures in all three studied systems. Moreover, the low temperature peaks present in the classical heat capacities of the clusters disappear in the quantum case (at least in the temperature range considered in this work).

ACKNOWLEDGMENTS

The authors acknowledge support from the National Science Foundation through Grant Nos. CHE-0095053 and CHE-0131114. One of us (D.S.) would like to thank Cristian Diaconu for helpful discussions. The authors would also like to thank Brown University's Center for Advanced Scientific Computing and Visualization for their assistance with the present research.

[1] S. Leutwyler and J. Bösiger, Chem. Rev. (Washington, D.C.) **90**, 489 (1990).
[2] U. Buck and I. Ettischer, J. Chem. Phys. **100**, 6974 (1994).
[3] J. Brudermann, U. Buck, and V. Buch, J. Phys. Chem. A **106**, 453 (2002).
[4] M. Schmidt, R. Kusche, W. Kronmüller, B. von Issendorff, and H. Haberland, Phys. Rev. Lett. **79**, 99 (1997).
[5] M. Schmidt, R. Kusche, B. von Issendorff, and H. Haberland, Nature (London) **393**, 238 (1998).
[6] R. Kusche, T. Hippler, M. Schmidt, B. von Issendorff, and H. Haberland, Eur. Phys. J. D **9**, 1 (1999).
[7] G. A. Breaux, R. C. Benirschke, T. Sugai, B. S. Kinnear, and M. F. Jarrold, Phys. Rev. Lett. **91**, 215508 (2003).
[8] R. S. Berry, T. L. Beck, H. L. Davis, and J. Jellinek, Adv. Chem. Phys. **70B**, 75 (1988).
[9] R. S. Berry, in *Theory of Atomic and Molecular Clusters*, edited by J. Jellinek (Springer, Berlin, 1999).

[10] C. Chakravarty, J. Chem. Phys. **102**, 956 (1995).

[11] C. Chakravarty, J. Chem. Phys. **103**, 10663 (1995).

[12] P. Shah, S. Roy, and C. Chakravarty, J. Chem. Phys. **118**, 10671 (2003).

[13] J. P. K. Doye, D. J. Wales, and M. A. Miller, J. Chem. Phys. **109**, 8143 (1998).

[14] F. Calvo and F. Spiegelmann, Phys. Rev. Lett. **82**, 2270 (1999).

[15] F. Calvo and F. Spiegelmann, J. Chem. Phys. **112**, 2888 (2000).

[16] F. Calvo, J. P. K. Doye, and D. J. Wales, J. Chem. Phys. **114**, 7312 (2001).

[17] C. J. Tsai and K. D. Jordan, J. Chem. Phys. **99**, 6957 (1993).

[18] J. M. Pedulla and K. D. Jordan, Chem. Phys. **239**, 593 (1998).

[19] L. J. Munro, A. Tharrington, and K. D. Jordan, Comput. Phys. Commun. **145**, 1 (2002).

[20] R. A. Christie and K. D. Jordan, J. Phys. Chem. B **106**, 8376 (2002).

[21] A. N. Tharrington and K. D. Jordan, J. Phys. Chem. A **107**, 7380 (2003).

[22] D. D. Frantz, J. Chem. Phys. **105**, 10030 (1996).

[23] D. D. Frantz, J. Chem. Phys. **107**, 1992 (1997).

[24] D. D. Frantz, J. Chem. Phys. **115**, 6136 (2001).

[25] D. D. Frantz, D. L. Freeman, and J. D. Doll, J. Chem. Phys. **97**, 5713 (1992).

[26] D. L. Freeman and J. D. Doll, Annu. Rev. Phys. Chem. **47**, 43 (1996).

[27] E. Curotto, D. L. Freeman, B. Chen, and J. D. Doll, Chem. Phys. Lett. **295**, 366 (1998).

[28] J. P. Neirotti, F. Calvo, D. L. Freeman, and J. D. Doll, J. Chem. Phys. **112**, 10340 (2000).

[29] A. J. Acevedo, L. M. Caballero, and G. E. López, J. Chem. Phys. **106**, 7257 (1997).

[30] G. E. López, J. Chem. Phys. **117**, 2225 (2002).

[31] D. Sabo, J. D. Doll, and D. L. Freeman, J. Chem. Phys. **121**, 847 (2004) (previous paper).

[32] F. Calvo, J. P. Neirotti, D. L. Freeman, and J. D. Doll, J. Chem. Phys. **112**, 10350 (2000).

[33] C. Predescu, D. Sabo, J. D. Doll, and D. L. Freeman, J. Chem. Phys. **119**, 12119 (2003).

[34] J. O. Hirschfelder, C. F. Curtiss, and R. B. Bird, *Molecular Theory of Gases and Liquids* (Wiley, New York, 1954), p. 168.

[35] J. K. Lee, J. A. Barker, and F. F. Abraham, J. Chem. Phys. **58**, 3166 (1973).

[36] J. P. Neirotti, D. L. Freeman, and J. D. Doll, Phys. Rev. E **62**, 7445 (2000).

[37] E. Marinari and G. Parisi, Europhys. Lett. **19**, 451 (1992).

[38] C. H. Geyer and E. A. Thompson, J. Am. Stat. Assoc. **90**, 909 (1995).

[39] U. H. E. Hansmann, Chem. Phys. Lett. **281**, 140 (1997).

[40] M. Falcioni and M. W. Deem, J. Chem. Phys. **110**, 1754 (1999).

[41] M. G. Wu and M. W. Deem, Mol. Phys. **97**, 559 (1999).

[42] Q. Yan and J. J. de Pablo, J. Chem. Phys. **111**, 9509 (1999).

[43] A. Srinivasan, D. M. Ceperley, and M. Mascagni, Adv. Chem. Phys. **105**, 13 (1999).

[44] http://archive.ncsa.uiuc.edu/Science/CMP/RNG/RNG-home.html

[45] C. Predescu, M. Predescu, and C. V. Ciobanu, J. Chem. Phys. **120**, 4119 (2004).

[46] M. Kalos and P. Whitlock, *Monte Carlo Methods* (Wiley, New York, 1986).

[47] C. Predescu, http://arXiv.org/abs/cond-math/0302171

[48] C. Predescu, D. Sabo, and J. D. Doll, J. Chem. Phys. **119**, 4641 (2003).

[49] C. Predescu and J. D. Doll, J. Chem. Phys. **117**, 7448 (2002).

[50] W. H. Press, S. A. Teukolsky, W. T. Vetterling, and B. P. Flannery, *Numerical Recipes*, 2nd ed. (Cambridge University Press, Cambridge, 1992).

[51] O. M. Becker and M. Karplus, J. Chem. Phys. **106**, 1495 (1997).

[52] D. J. Wales, J. P. K. Doye, M. A. Miller, P. N. Mortenson, and T. R. Walsh, Adv. Chem. Phys. **115**, 1 (2000).

[53] J. P. K. Doye, M. A. Miller, and D. J. Wales, J. Chem. Phys. **111**, 8417 (1999).

[54] J. P. K. Doye and F. Calvo, J. Chem. Phys. **116**, 8307 (2002).

[55] J. P. Neirotti, D. L. Freeman, and J. D. Doll, J. Chem. Phys. **112**, 3990 (2000).

The Journal of Chemical Physics is copyrighted by the American Institute of Physics (AIP). Redistribution of journal material is subject to the AIP online journal license and/or AIP copyright. For more information, see http://ojps.aip.org/jcpo/jcpcr/jsp
Copyright of Journal of Chemical Physics is the property of American Institute of Physics and its content may not be copied or emailed to multiple sites or posted to a listserv without the copyright holder's express written permission. However, users may print, download, or email articles for individual use.

The Journal of Chemical Physics is copyrighted by the American Institute of Physics (AIP). Redistribution of journal material is subject to the AIP online journal license and/or AIP copyright. For more information, see http://ojps.aip.org/jcpo/jcpcr/jsp